Monthly Notices
of the
ROYAL ASTRONOMICAL SOCIETY

MNRAS **489,** 5231–5243 (2019) doi:10.1093/mnras/stz2280

Low-mass nitrogen-, oxygen-bearing, and aromatic compounds in Enceladean ice grains

N. Khawaja,[1,2]★ F. Postberg,[1,2] J. Hillier,[1] F. Klenner,[1,2] S. Kempf,[3] L. Nölle,[1,2] R. Reviol,[2] Z. Zou[1] and R. Srama[4]

[1] *Institut für Geologische Wissenschaften, Freie Universität Berlin, Malteserstraße 74-100, D-12249 Berlin, Germany*
[2] *Institut für Geowissenschaften, Universität Heidelberg, Im Neuenheimer Feld 234-236, D-69120 Heidelberg, Germany*
[3] *Laboratory for Atmospheric and Space Physics, University of Colorado, 1234 Innovation Dr, Boulder, CO 80303, USA*
[4] *Institut für Raumfahrtsysteme, Universität Stuttgart, Pfaffenwaldring 29, D-70569 Stuttgart, Germany*

Accepted 2019 August 8. Received 2019 July 15; in original form 2018 December 21

ABSTRACT

Saturn's moon Enceladus is erupting a plume of gas and ice grains from its south pole. Linked directly to the moon's subsurface global ocean, plume material travels through cracks in the icy crust and is ejected into space. The subsurface ocean is believed to be in contact with the rocky core, with ongoing hydrothermal activity present. The Cassini spacecraft's Ion and Neutral Mass Spectrometer (INMS) detected volatile, gas phase, organic species in the plume and the Cosmic Dust Analyser (CDA) discovered high-mass, complex organic material in a small fraction of ice grains. Here, we present a broader compositional analysis of CDA mass spectra from organic-bearing ice grains. Through analogue experiments, we find spectral characteristics attributable to low-mass organic compounds in the Enceladean ice grains: nitrogen-bearing, oxygen-bearing, and aromatic. By comparison with INMS results, we identify low-mass amines [particularly (di)methylamine and/or ethylamine] and carbonyls (with acetic acid and/or acetaldehyde most suitable) as the best candidates for the N- and O-bearing compounds, respectively. Inferred organic concentrations in individual ice particles vary but may reach tens of mmol levels. The low-mass nitrogen- and oxygen-bearing compounds are dissolved in the ocean, evaporating efficiently at its surface and entering the ice grains via vapour adsorption. The potentially partially water soluble, low-mass aromatic compounds may alternatively enter ice grains via aerosolization. These amines, carbonyls, and aromatic compounds could be ideal precursors for mineral-catalysed Friedel–Crafts hydrothermal synthesis of biologically relevant organic compounds in the warm depths of Enceladus' ocean.

Key words: astrobiology – astrochemistry – planets and satellites: individual: Enceladus – planets and satellites: oceans.

1 INTRODUCTION

One of the many spectacular discoveries made by the Cassini–Huygens mission was a plume of icy particles and vapour emitted from the Saturn's moon Enceladus (Dougherty et al. 2006; Hansen et al. 2006; Porco et al. 2006; Spahn et al. 2006a), connected to a global subsurface ocean (Thomas et al. 2016). Ocean material is ejected in the form of gas (Hansen et al. 2006, 2011; Waite et al. 2006, 2009, 2017) and water–ice-dominated grains (Hillier et al. 2007; Postberg et al. 2008, 2009a, 2011, 2018a; Hsu et al. 2015) from Enceladus, through warm cracks in the Enceladean south polar ice crust (Spencer et al. 2006). Most of the emitted ice grains are too slow to leave the moon's Hill sphere, and fall back on to the surface (Kempf, Beckmann & Schmidt 2010; Southworth, Kempf & Spitale 2019). However, approximately 5–10 per cent of the emitted ice grains escape and enter the Saturn's diffuse E ring (Spahn et al. 2006b; Kempf et al. 2010, 2018).

Cassini's mass spectrometers – Ion and Neutral Mass Spectrometer (INMS) and Cosmic Dust Analyser (CDA) – have analysed ejected materials both inside the plume and the E ring. The discovery by CDA of sodium salts in E ring ice grains provided evidence that the Enceladean subsurface ocean is/was in contact with the rocky core (Postberg et al. 2009a, 2011) and constrained the ocean's moderate salinity and alkaline pH. The detection of nanometre-sized silica (SiO_2) particles in the E ring strongly suggested ongoing

★ E-mail: nozair.khawaja@fu-berlin.de

hydrothermal activity at Enceladus' subsurface ocean (Hsu et al. 2015) and provided further evidence that the ocean has a relatively high pH. The detection of molecular hydrogen and methane by INMS not only confirmed subsurface water–rock interaction but also provided further evidence for serpentinization reactions, an exothermic, hydrogen-producing geochemical process (Waite et al. 2017). The hydrothermal activity is thought to occur inside the water-percolated, porous, rocky core of the moon (Sekine et al. 2015; Waite et al. 2017) and is probably maintained by heat generated by tidal dissipation (Choblet et al. 2017).

The CDA records time-of-flight (TOF) mass spectra of cations generated by high-velocity ($v \geq 3$ km s^{-1}) impacts of individual grains on to a rhodium target (Srama et al. 2004). Previous analyses inferred three different spectral types of Enceladean ice grains (Postberg et al. 2008, 2009a): Type 1 represents grains of almost pure water ice, Type 2 shows features consistent with grains containing significant amounts of organic material, and Type 3 is indicative of salt-rich water ice grains. This work focusses on a detailed analysis of Type 2 grains.

In contrast to Type 1 and Type 3, Type 2 spectra exhibit a more diverse compositional range, indicating the existence of different compositional subclasses and a wide variety of concentrations of organic compounds. A small subpopulation of Type 2 grains with specific spectral features (repetitive peaks, separated by 12–13 u in mass, extending from 80 u until at least CDA's high-mass limit of approx. 200 u, known as High-Mass Organic Cations, HMOC) has already been investigated by Postberg et al. (2018a). The spectra were interpreted as due to ice grains carrying complex organic material, which had parent molecular masses in excess of 200 u at concentrations on the per cent level. The study provided evidence for the existence of aromatic and aliphatic substructures, identified as unsaturated and saturated cation fragments of the high-mass complex organic material, as well as oxygen-bearing functional groups in these grains. It was suggested that the detected high-mass organics originate from poorly soluble material concentrated in an organic-rich layer at the top of Enceladus' oceanic water table.

2 MOTIVATION

Postberg et al. (2018a) discussed possible exogenic and/or endogenic origins for the HMOC material on Enceladus. In the former case, the accretion of primordial organic material during the formation of Enceladus from planetesimals delivered organic matter into the core, from whence it subsequently leached. The HMOC material would then be similar to the insoluble organic matter (IOM) observed in meteorites (e.g. Alexander et al. 2017). Alternatively, endogenous HMOC material could be hydrothermally synthesized (Vinogradoff et al. 2018) from lower mass compounds on Enceladus. This poorly soluble high-mass organic material identified by Postberg et al. (2018a) is, however, unlikely to be a reactant, but may be a product of such syntheses involving lower mass, soluble O- and N-bearing polar molecules. With the new data presented in this work, we investigate the contribution of hydrothermal processes to Enceladus' organic inventory.

Laboratory synthesis of amino acids from simple carbonyl (oxygen-bearing) compounds in a simulated hydrothermal vent environment has been shown to occur (Barge et al. 2019). Furthermore, a protein-forming N-bearing aromatic amino acid, Tryptophan, whose formation is believed to be catalysed by clay minerals, has been found in the alkaline environment of Lost City hydrothermal field (Ménez et al. 2018). The identification of low-mass, polar organics within the Enceladean ocean would be an indicator that such reactions may occur and place constraints on the hydrothermal environment at and below the core-ocean boundary. Magee & Waite (2017) tentatively identify possibly soluble O- and N-bearing organic species in the gas phase emerging from Enceladus ocean. However, no unquestionable evidence of such compounds, other than those that could be fragments from higher mass species (Postberg et al. 2018a), has thus far been found on Enceladus.

In this work, we present a compositional analysis of CDA spectra of Type 2 grains to find and identify the compositional families, including functional groups, of low-mass soluble organics, henceforth 'volatile organic compounds' (VOCs), in the ice grains emitted from Enceladus' subsurface ocean. The spectral analysis (Section 4) is supported by a laser-driven analogue experiment [Supplementary Material (SM) section A] simulating the impact ionization process and the resulting mass spectra of ice particles (Postberg et al. 2009a, 2018a; Klenner et al. 2019). To identify the observed patterns of cationic organic fragments in Type 2 spectra containing VOCs, we have measured spectra of a large number of water-dissolved organic compounds (Section 4 and Tables SM 1, 2, and 3). After a brief summary (Section 5), we discuss our results and their implications for Enceladus (Sections 6 and 7).

3 THE DATA SET

We have investigated 731 Type 2 spectra (SM section B) of Enceladean ice grains, recorded in the E ring between 2004 November and 2008 May. The spectra were calibrated on to a mass scale, via identification of the hydronium (H_3O^+), sodium (Na^+), and water-cluster peaks [$(H_2O)_nH_3O^+$], using bespoke software developed for CDA data analysis (spectrumgui, pers. comm. S. Kempf). This process typically resulted in mass uncertainties of <0.5 u at masses below 80 u, rising to 1–2 u between 80 and 180 u (Postberg et al. 2018a).

These spectra were produced at Saturnian distances of between $\sim$3.5 and 17 Rs (Saturnian radii, Rs = 60 268 km) and at impact speeds of between $\sim$4.5 and 15 km s^{-1}. The speed determination is based on the idealized assumption that particles are on prograde circular orbits in the E ring. In reality, the eccentricities of E ring grains introduce uncertainties in impact speeds that scatter around the assumed values for circular orbits.

In addition to water-cluster cations of the form $H_3O^+(H_2O)_{1\text{-}8}$ (Fig. 1), typical for all salt-poor water ice impacts (Hillier et al. 2007; Postberg et al. 2008), many Type 2 spectra are characterized by a broad peak (corresponding to a set of mass lines between 26 and 31 u), in agreement with multiple indistinguishable cationic organic fragments (e.g. $C_2H_{3,5}^+$, $CH_{1,2,3}O^+$, $CH_{0,1,2}N^+$), which we will henceforth call the Type 2 Low-Mass Organic Signature (LMOS). Postberg et al. (2008) used this spectral feature as the defining criterion for Type 2 classification. Furthermore, most Type 2 spectra also exhibit a broad feature between 39 and 45 u, which often appears on the right flank of the second water-cluster peak (Fig. 1). Like LMOS, this signature can potentially be attributed to a number of different organic cations, which cannot be distinguished with the CDA's mass resolution: hydrocarbons ($C_3H_{3,5,7}^+$), N-bearing ($C_2H_{2,4}NH_2^+$), or O- and OH-bearing ($C_2H_{3,5}O^+$) cations. We therefore widen the definition of Type 2 spectra from Postberg et al. (2008), by requiring the LMOS and/or the extended broad feature between 39 and 45 u to be present with a signal-to-noise ratio of at least 2.5σ.

For this work, we have specifically searched for additional spectral features in the data set that, in contrast to the general features described above, enable the identification of specific functional and

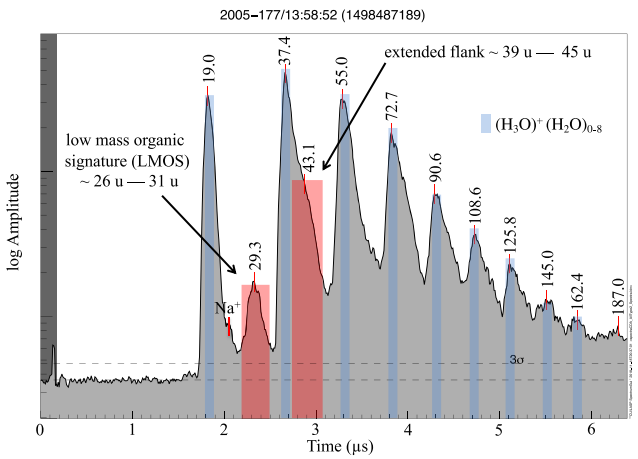

Figure 1. A typical Type 2 spectrum with the two defining features (indicated by the broad red bars). The first one occurs between 2.2 and 2.5 μs, typically covering a mass range of 26 and 31 u, and is labelled as the low-mass organic signature (LMOS). The second feature is an extended right flank (between 2.7 and 3.1 μs) of the second water cluster ($H_3O^+H_2O$). It ranges from 39 to 45 u but is not detached from the neighbouring water peak in most cases (Postberg et al. 2008). Marked in blue are hydronium (19 u) and water-cluster cations at 37, 55, 73, 91, 109, 127, 145, and 163 u. Na^+ is visible on the right of hydronium. Peak labels here and in subsequent spectra are in unified atomic mass units (u).

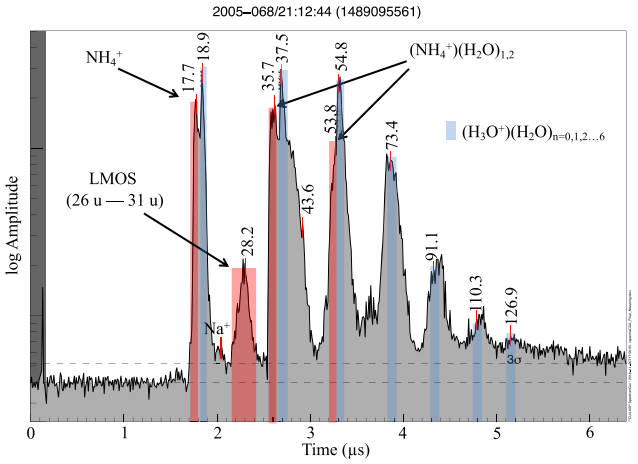

Figure 2. A single CDA TOF mass spectrum from a N-bearing E ring ice grain. The spectrum exhibits signatures of N-bearing ions generated by the approx. 8.5 km s^{-1} impact of an E ring ice grain at a Saturnian distance of 7.2 Rs. The red markers indicate ammonium cations (NH_4^+, 18 u), the Type 2 characteristic organic signature (LMOS) and possible ammonium-water clusters at 36 and 54 u, respectively. On the right and left flanks of some water clusters, unresolved features possibly represent cations arising from other organic species.

structural characteristics of organic compounds. Despite CDA's rather low mass resolution (Srama et al. 2004; Postberg et al. 2008), these specific features are visible as separate peaks, because they are formed by abundant organic cations with masses that do not interfere with the omnipresent water-cluster peaks. We have identified three such specific features occurring in a relatively large number of Type 2 spectra and selected those spectra that show at least one of these features with high significance (SM section B) to use as templates for reproduction with our analogue experiments.

In total, about 8 per cent (60) of the investigated Type 2 spectra in the data set (Table SM 4) fulfilled our strict selection criteria (SM section B) for one of the three distinct organic features, which we used to infer a specific composition. In the following, we will refer to this exemplary subset as 'archetypal' Type 2 spectra. The organic compounds we identify in the archetypes are probably present in a much larger fraction of the E ring ice grains, but may not be unambiguously detected at lower concentrations or if subject to interference with mass lines arising from other grain constituents.

4 SPECTRAL ANALYSIS AND INTERPRETATION

The following spectral analysis is separated according to the three aforementioned archetypal subsets, each with different spectral characteristics. Generally, the specific signatures are in agreement with organic fractions in these grains up to the tens of mmol L^{-1} level, as inferred from our analogue experiments with pure organic compounds in water (Tables SM 1, 2, and 3).

4.1 N-bearing Type 2 spectra (Type 2N)

Approximately 33 per cent of the subset of archetypal Type 2 spectra (Table SM 4) shows a significant peak at 18 u that, based on our selection criteria (SM section B1), is attributed to ammonium cations, NH_4^+. Henceforth, we name this nitrogen-bearing subtype

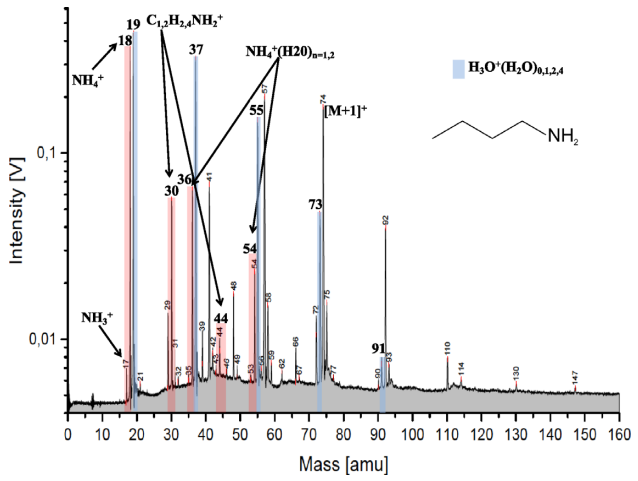

Figure 3. Laser ionization analogue laboratory spectrum of an aqueous solution of butyl amine at a concentration of 0.05 mol L^{-1}. NH_4^+, $CH_2NH_2^+$, $C_2H_4NH_2^+$, and water clusters with NH_4^+ are marked in red at 18, 30, 44, 36, and 54 u, respectively. A minor contribution from NH_3^+ is also visible at 17 u. The protonated molecular peak of butyl amine appears at 74 u and it forms water clusters at 92 and 110 u. The pure water-cluster species present at 19, 37, 55, 73, and 91 u are marked in blue.

of Type 2 spectra as 'N-bearing', or Type 2N (Fig. 2). In some cases, 18 u appears in spectra together with peaks at 36 u and/or 54 u, which can be attributed to ammonium-water-cluster species $NH_4^+(H_2O)_{1,2}$. Fig. 2 shows a typical example of such a spectrum. In our analogue laboratory set-up (SM section B1), we obtain a NH_4^+ peak at 18 u as the strongest fragment signature arising from a wide variety of amine, amide, and nitrile compounds (Table SM 1). As an example, butyl amine (Fig. 3) is shown. Heterocyclic N-bearing species do not yield a substantial NH_4^+ peak (Table SM 1) and can be ruled out as a source here.

Another fragment peak at 30 u due to methaniminium cations ($CH_2NH_2^+$) is also observed in the laboratory. However, the 30 u

peak cannot be isolated from the broad (approx. 26–31 u) LMOS feature in CDA spectra. A minor peak at 44 u is attributed to $C_2H_4NH_2^+$ (Fig. 3), but in most CDA spectra this feature is also not resolved (Figs 1 and 2). The ammonium-water clusters are clearly recognizable at 36 and 54 u. On rare occasions, a minor peak at 17 u, as shown in the laboratory spectrum (Fig. 3), was also observed in CDA spectra and can be attributed to NH_3^+. In principle, H_2O^+ may appear as an isobaric species to NH_4^+ at 18 u as H_2O^+ is known to appear as a minor species conjointly with hydronium cations (H_3O^+) (Donsig & Vickerman 1997; Buratti et al. 2019). However, this minor water ion occurs only at high impact speeds (SM section B1). In order to distinguish NH_4^+ from H_2O^+, we only considered spectra that exhibited a high abundance of the 18 u species at low impact speeds (SM section B1). This ensures that, in the subsample of Type 2 spectra considered here, the 18 u peak is dominated by NH_4^+.

4.2 O-bearing Type 2 spectra (Type 2O)

This subgroup of Type 2 spectra [∼40 per cent of archetypal Type 2 spectra (O-bearing or Type 2O, Table SM 4)] is characterized by a distinct, isolated, peak either at 43 u or at 45 u, which we attribute to $C_2H_3O^+$ (acylium) and $C_2H_5O^+$, respectively (Fig. 4). These are well-known characteristic cationic fragments of organic parent molecules in which oxygen is double bonded, or hydroxyl or oxygen are single bonded, to carbon. Ice grain impacts that fulfil these selection criteria for O-bearing spectra (SM section B2) have been detected only at impact speeds below ∼8.5 km s^{-1}.

As already discussed in Postberg et al. (2018a) for the high-mass organic material, a peak at 45 u cannot originate from pure hydrocarbons and requires a heteroatom from hydroxyl, ethoxy, or carbonyl functional groups. This is also true for the low-mass organics investigated here and a prominent example is shown in Fig. 4(a).

In this work, we additionally assign the peak at 43 u in certain spectra as arising from oxygen-bearing cations Fig. 4(b). In contrast to the extended flank-feature between 38 and 45 u, characteristic for many Type 2 spectra (Fig. 1) and which probably derives from a multitude of species, the oxygen-bearing spectra discussed here are characterized by discrete, isolated peaks at 43 u.

To investigate this spectral feature, a wide variety of oxygen-bearing organic compounds were analysed (Table SM 2) with the analogue experiment. Most investigated species with carbonyl and/or hydroxyl functional groups produced an intense peak at 43 u together with a relatively minor peak at 45 u. As an example, the laboratory spectrum of butanal is shown in Fig. 5, in which a 43 u peak arising mainly from acylium cations ($C_2H_3O^+$) is clearly visible together with a conjoint minor peak at 45 u ($C_2H_5O^+$). The 43 u peak was also reproduced with aromatic species in which a short O-bearing aliphatic chain is attached to an aromatic ring structure (Table SM 2).

A potential interference with the acylium ion can arise from larger aliphatic chains efficiently forming C_3 hydrocarbon fragments ($C_3H_{3\text{-}7}^+$). However, several observations, most notably the absence of the conjoint minor peaks at 45 and 30–31 u (see below) argues for O-bearing cations being predominant. But a contribution of $C_3H_7^+$ at *m/z* 43 as an addition to $C_2H_3O^+$ is possible. For a detailed discussion of this interference, we refer to SM section B2.

In some O-bearing CDA spectra, the LMOS feature shows a tendency to peak towards the higher end of its typical mass range (26–31 u), in agreement with the presence of formyl cations ($CH_{2,3}O^+$, 30 u, 31 u). At the low (≤8.5 km s^{-1}) velocities

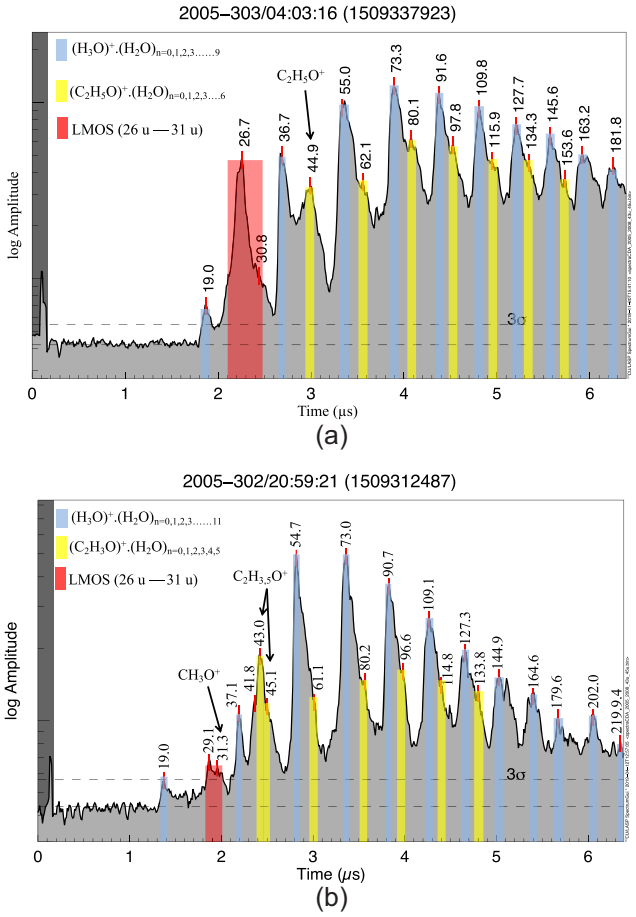

Figure 4. CDA TOF mass spectra of E ring ice grains with characteristic cationic fragments from O-bearing organics. Spectrum (a) was recorded at a Saturnian distance of 5.6 Rs by a particle impacting at ∼6.5 km s^{-1}. In this case, the characteristic O-bearing fragments are $C_2H_5O^+$ cations at 45 u. Spectrum (b) was recorded at a Saturnian distance of 5 Rs, generated by a particle impacting at ∼5 km s^{-1}. In this spectrum, the characteristic O-bearing fragments are acylium cations ($C_2H_3O^+$, 43 u) indicative of carbonyl or hydroxyl functional groups. In both (a and b) examples, formyl cations (CH_3O^+, 31 u) as a supporting evidence of O-bearing species are also visible. Water clusters are indicated by the blue bars, with the large red bars highlighting the Type 2 low-mass organic signature (LMOS). Marked in yellow are the characteristic O-bearing cations and their water clusters. All other signatures that are not marked or colour shaded are mostly due to organic species or organic-bearing water clusters.

considered here, we discount the formation of these peaks via carbon-water clustering (Hillier et al. 2007; Postberg et al. 2009b and SM section B2) or as a cation fragment of alcohols as suggested by Postberg et al. (2008), as this is not supported by our laboratory analogue spectra. The conjoint production of the cationic fragments $C_2H_{3,5}O^+$ and $CH_{2,3}O^+$ from O-bearing compounds is however described in, e.g. McLafferty & Turecek (1993) and Lee (1998) and has also been observed in carbonyl-bearing spectra from an icy matrix (Henderson & Gudipati 2015). We confirm this with our analogue experiment (Fig. 5) where the acylium ion at 43 u appears conjointly with the formyl cationic peak at 31 u.

The amplitudes of the hydronium peak at 19 u and the water-cluster feature at 37 u are significantly lower with respect to the water cluster at 55 u in most 2O spectra. This is unusual for Type 2 spectra where the low-mass water peaks (19 u, 37 u) occur at similar

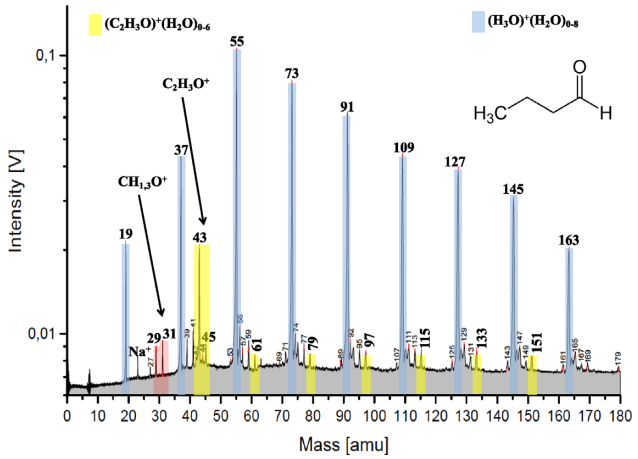

Figure 5. Laboratory TOF spectrum of an aqueous solution of butanal at a concentration of 0.15 mol L^{-1}. Hydronium/water-cluster cations and acylium ($C_2H_3O^+$, 43 u) cations are shown in blue and yellow, respectively. The pair of peaks marked in red can originate from formyl cations ($CH_{1,3}O^+$). Although the 29 u peak can also be formed from hydrocarbon cations, that at 31 u is only produced by an oxygen-bearing fragment and can be used as further supporting evidence for the inference of O-bearing organics.

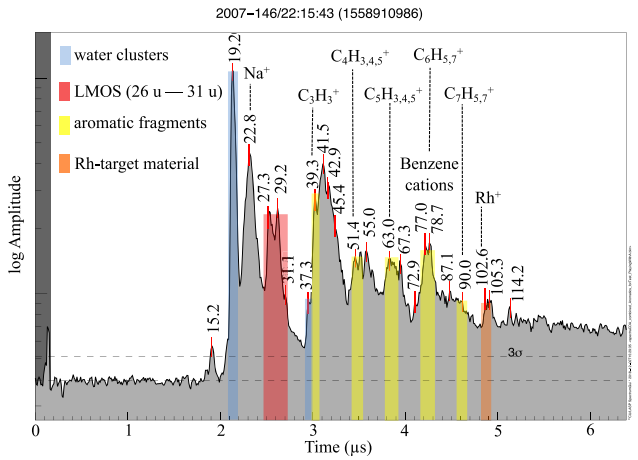

Figure 6. A TOF impact mass spectrum representing an archetypal aromatic-type spectrum (2A) recorded at an impact speed of ~10 km s^{-1} at 3.6 Rs. Different signatures are colour shaded. Pure-water clusters at 19 and 37 u, typical Type 2 features between mass ranges ~26 and 31 u, aromatic cationic fragments $C_3H_3^+$ (39 u), $C_4H_{3,4,5}^+$ (51–53 u), $C_5H_{3,4,5}^+$ (63–65 u), $C_6H_{5,7}^+$ (77 u, 79 u), $C_7H_7^+$ (91 u), and rhodium target cations Rh^+ (103 u) are indicated by blue, red, yellow, and orange bars, respectively. All other signatures that are not colour shaded are mostly due to organic cations. We note that the Na-water cluster (H_2O-Na^+, 41 u) might coincide with the C_3H_5 cation, and a further organic cation might also coincide with Rh^+.

or higher amplitudes than the one at 55 u (see Figs 1, 2, and 6 for comparison).

In a few cases, McLafferty rearrangement (see section SM B2), in which (M-OH) cations at mass 55 u are formed via the cleavage of the OH functional group formed by the transfer of hydrogen on to the oxygen, may be responsible for the increased intensity of 55 u peak. However, it is also possible that the 19 and 37 u peak amplitudes are instead being suppressed. This is a known phenomenon in, e.g. matrix-assisted laser desorption/ionization (MALDI), often seen with high concentrations of organics (Knochenmuss et al. 1996), or salts (Piwowar, Lockyer & Vickerman 2009) and referred to as a matrix effect.

4.3 Aromatic-bearing Type 2 spectra (Type 2A)

Postberg et al. (2018a) found high mass organic cations (HMOC) appearing at masses above 80 u in spectra of E ring ice grains, with these spectral features always coinciding with aromatic cationic fragments. However, the reverse is not always true: aromatic features do not necessarily coincide with HMOC. In this section, we consider CDA Type 2 spectra, defined as aromatic-bearing 2A, in which aromatic features do not appear with HMOC.

Aromatic-type (or Type 2A) spectra (approx. 45 per cent archetypal Type 2 spectra; Table SM 4) show a broad but distinct peak at ~77–79 u, indicative of benzene-derived fragments (Fig. 6) such as the phenyl ($C_6H_5^+$, 77 u) and benzenium ($C_6H_7^+$, 79 u) cations (SM section B3). A coincident peak often appears at masses 89–91 u, which we attribute to tropylium ($C_7H_7^+$, 91 u) and dehydrotropylium cations ($C_7H_5^+$, 89 u). As with the observations by Postberg et al. (2018a), the peak amplitude of tropylium is always lower than those due to phenyl cations. These aromatic features may coincide with cation peaks at *m/z* 63–65 u, 51–53 u, and 39 u (Fig. SM 6). These species ($C_5H_{3,4,5}^+$, $C_4H_{3,4,5}^+$, and $C_3H_3^+$) are known as the aromatic cationic fragment series (e.g. McLafferty & Turecek 1993). The aromatic fragments of Type 2A appear in spectra obtained over a broad range of impact speeds – from 6 to 15 km s^{-1}, thus often appearing at notably higher speeds than Type 2N and 2O. Amongst several aromatic compounds (Table SM 3) tested in the analogue experiment, only monocyclic aromatic compounds (MACs) resulted in the formation of the observed aromatic cationic fragment series.

The phenyl and benzoyl group compounds of MAC efficiently produce phenyl and/or benzenium cations ($C_6H_{5,7}^+$), and benzyl group compounds produce significant abundances of tropylium cations ($C_7H_7^+$), whereas this is not observed for compounds with fused benzene rings, e.g. pyrene (Postberg et al. 2018a). In Type 2A spectra, phenyl cations are more abundant than tropylium cations. The laboratory experiments (SM section B3) indicate the preferred formation of phenyl cations when an aromatic ring is directly attached to a non-alkyl (or dehydrogenated) functional group, e.g. aniline (C_6H_5-NH_2) and benzoic acid (C_6H_5-COOH). In addition, untested, non-polar, styrene-like ($C_8H_8^+$) MAC(s) might also produce significant abundances of phenyl cations as seen in CDA Type 2A spectra. These substances would be expected to yield clear molecular peaks (94 and 123 u for the polar examples, 105 u for the non-polar) with amplitudes comparable to that of the generated phenyl cations. That this is not observed in CDA Type 2A spectra thus limits the contributions of these particular compounds, leaving benzene as the most likely abundant suitably soluble compound that could give rise to the defining peak(s) at 77–79 u.

The nominal period of CDA spectral recording is 6.4 µs after the instrument is triggered. However, CDA also has an extended mass range, from 6.4 µs up to 40 µs, with an extremely low mass resolution. It is noteworthy that in a few cases, Type 2A spectra have a significant signal within this extended mass range, as has been more frequently observed in HMOC spectra (Postberg et at. 2018a). In these cases, the presence of molecules with masses >200 u in parallel with MAC in the grains is indicated. However, in contrast to the HMOC spectra discussed in Postberg et al. (2018a), in Type 2A it is highly unlikely that the MACs are impact fragments of the high-mass species because (unlike HMOC spectra) the 2A spectra do not

show any indication of periodic patterns of fragment cations above 91 u. It is, though, still possible that the compounds contributing to Type 2A spectra are low-mass poorly soluble aromatics (e.g. styrene), perhaps associated with the HMOC material.

4.4 Mixed-type spectra (Type 2 M)

17 per cent of archetypal CDA Type 2 spectra (Table SM 4) exhibit features indicative of a combination of more than one of the three subtypes (Table 1 and Table SM 4), based on our conservative selection criteria (SM section B). The following combinations are observed:

Aromatic + O-bearing: Occasionally, aromatic cation peaks ($C_{6,7}H_{5,7}^+$) are observed with an additional oxygen-bearing peak ($C_2H_3O^+$ and/or $C_2H_5O^+$) at 43 and/or 45 u.

Aromatic + N-bearing: Similarly, the aromatic cations ($C_{6,7}H_{5,7}^+$) sometimes coincide with the defining feature (NH_4^+) of N-bearing species.

O-bearing + N-bearing: These mixed spectra exhibit characteristic fragments of O- ($C_2H_3O^+$ and/or $C_2H_5O^+$) and N-bearing (NH_4^+) species.

Aromatic + O-bearing + N-bearing: Some mixed-type spectra also combine the characteristic features ($C_{6,7}H_{5,7}^+$, $C_2H_3O^+$/$C_2H_5O^+$ & NH_4^+) of all three subtypes.

Accurate analyses of mixed-type spectra (Type 2 M) are complicated by the presence of significant numbers of further, often interfering, spectral peaks arising from the multiple organic species. However, the features attributable to N- and O-bearing, as well as aromatic-type, compounds are clearly visible in these spectra.

4.5 Re-analysis of the HMOC data set

In addition to the data set with low-mass organic compounds outlined in Section 3, we also reinvestigated the HMOC data set of Postberg et al. (2018a) to look for evidence of N- and O-bearing features. Postberg et al. (2018a) already tentatively attributed 45 and 44 u peaks to $C_2H_5O^+$ and $C_2H_6N^+$, respectively. Additionally, we now find further evidence of N-bearing and O-bearing species in HMOC-type spectra by identifying NH_4^+ (18 u) and $C_2H_3O^+$ (43 u) (Figs SM 7 and 8). This finding verifies the previously tentative identifications of Postberg et al. (2018a).

5 RESULTS

In the following, we summarize the results from the preceding spectral analyses and consider their implications for the composition of E ring grains.

To infer the functional and structural characteristics of organic compounds despite the low mass resolution of CDA, we only considered spectra in which specific, identifiable, high-significance, features occurred, i.e. archetype spectra. This subset amounts to ~8 per cent of the Type 2 spectra considered for this work. However, there are many additional spectra where these characteristics are indicated but which did not fulfil our conservative selection criteria (SM section B). It is therefore very likely that all three organic compositional properties discussed in this work occur in a much larger fraction of the ice grains, but at concentrations not allowing unmistakable identification, or obstructed by spectral interferences with other organic features. Organic species isobaric (at CDA's mass resolution) with water clusters or those that do not efficiently form cations will remain undetected in spectra, even if present in relatively high concentrations.

Furthermore, in this work, we only considered organic signatures that are relatively frequent (>2 per cent of all Type 2 spectra analysed so far). Other classes of organic compounds that may produce features less frequently observed in CDA mass spectra will be the subject of future work.

The mixed-type spectra may indicate that multiple simple organic compounds coexist in the ice grains. However, it is also feasible that a single, more complex, compound produces such features. For example, the presence of aromatic compounds with an attached short aliphatic chain containing a carbonyl/ethoxy/OH functional group, or two different organic compounds (i.e. carbonyl and aromatic) in a single ice grain. Our stringent selection criteria (SM section B) result in a very low number of this spectral type. It is therefore likely that a larger number of ice grains contain more than one of these functional groups, perhaps in combination with other currently unknown organic compounds.

Table 1 summarizes the spectral properties of the observed organic compounds in the ice grains. A concentration of organic species of at least a few mmol L^{-1} is required to produce spectral features in the laboratory that match those seen in the archetypal CDA spectra. In particular, for some O-bearing spectra, concentrations above 0.05 mol L^{-1} are required to produce the detected enhancement in the amplitude of the 55 u peak (Fig. SM 3).

The spectra of N- and O-bearing organics (Figs 2 and 4) are indeed indicative of VOCs – low-mass (<60 u), polar and hydrophilic, compounds. In contrast to the high-mass, insoluble, organic material (Postberg et al. 2018a), these are likely to be soluble in the ocean water. McLafferty rearrangement indicative of carbonyl compounds with at least four carbon atoms (SM section B2) is rarely observed, arguing against the presence of abundant species with four or more carbon atoms. We discount inorganic N-bearing sources of ammonium cations, such as N-bearing inorganic minerals (e.g. ammonium salts) or gaseous ammonia, as significant contributors to the N-bearing spectral signatures. NH_4^+ is only observed in high abundance together with other organic fragments, minimizing the possibility of an inorganic origin. Energetic arguments (desorption temperature and binding energy) make it unlikely that ammonia gas will enter grains at temperatures above 145 K (He, Acharyya & Vidali 2016; SM section B1). Furthermore, the archetypal N-bearing spectra show no indication of other abundant inorganic species (e.g. Na) as observed in the case of salt-rich Type 3 grains (Postberg et al. 2009a).

In ice grains belonging to the aromatic subtype (2A), phenyl- (excluding toluene) and/or benzoyl-rich aromatic compounds are in higher abundance than benzyl-rich compounds, leading to the observed increased abundance of phenyl cations in comparison to tropylium (Fig. SM 5). Cassini's INMS provided evidence of benzene-like aromatic fragments $C_6H_{5\text{-}7}$ in the Enceladean plume, probably from fragmentation of larger organic compounds residing in ice grains (Postberg et al. 2018a).

Our reinvestigation of the HMOC data set originally analysed by Postberg et al. (2018a) affirms that macro-molecular material identified there appears together with N- and O-bearing functional groups (Figs SM 7 and 8). It is possible that HMOC-material coexists with separate N- and O-bearing organic species mixed within the same grains. However, a further plausible explanation is that the HMOC material itself carries abundant O- and N-bearing functional groups.

Table 1. Summary of spectral properties of subtypes of organic-enriched ice grains. Percentage of each subtype is given with respect to the total archetypal CDA Type 2 spectra (column X) and all Type 2 spectra (column Y) considered here. Note that percentages may total greater than 100 due to overlap between M and individual, N, O, A subtypes.

Type 2 subtypes	X (per cent)	Y (per cent)	Identifying cations	Interpretation
N (N-bearing)	33	2.7	Main: NH_4^+ Supporting: $NH_4^+(H_2O)_{1,2}$	N-bearing organic molecules probably aliphatic. Candidate molecules: amines, nitriles, or amides.
O (O-bearing)	40	3.3	Main: $C_2H_{3,5}O^+$ Supporting: $CH_{1,2,3}O^+$	O-bearing organic molecules: carbonyl, ethoxy/hydroxyl. LMOS feature often shifted to 29–31 u possibly due to formyl cations.
A (Aromatic)	45	3.7	Main: $C_6H_{5,7}^+$, $C_7H_{5,7}^+$ Supporting: $C_3H_3^+$, $C_4H_{3,5}^+$, $C_5H_{3,5}^+$	The series of unsaturated cationic species indicates aromatic compounds. High abundance of benzene-like cations ($C_6H_{5,7}^+$) compared to tropylium cations ($C_7H_{5,7}^+$) suggests the existence of benzene, phenyl and/or benzoyl-like aromatic compounds.
M (Mixed)	17	1.4	N+O, O+A, A+N & N+O+A	Characteristic cations of more than one subtype appear together in this category. This implies the presence of either a single compound with multiple characteristics, or the coexistence of multiple compounds carrying different functional groups.

6 DISCUSSION

This new understanding of oxygen- and nitrogen-bearing low-mass organic compounds found in Enceladean ice grains has important implications for the composition of Enceladus' subsurface ocean, and the mechanisms of grain formation from it. Postberg et al. (2018a, 2018b) argue that the detected complex organic molecules discussed in their work originate from Enceladus' hydrothermal core. Indeed, hydrothermal processes on the Earth are known to be capable of producing complex organics, and similar processes may occur within Enceladus (Baross 2018). The serpentinizing environment of Enceladus' water–rock system as suggested by, e.g. Hsu et al. (2015), Sekine et al. (2015), and Waite et al. (2017) implies conditions (pH and temperature) similar to the Lost City hydrothermal system under the mid-Atlantic Ocean (Tobie 2015), in which Ménez et al. (2018) found evidence for the presence of a nitrogen-bearing, aromatic amino acid – tryptophan.

Multiple iron-containing minerals have been found to catalyse organic reactions in hydrothermal-like environments. The clay mineral, saponite, is thought to be a catalyst for the synthesis of heterocyclic amino acids, and other organic molecules including pyrimidine and pyrine (Baross 2018), which are the nitrogenous basis of DNA and RNA. As well as the generation of small molecules like tryptophan, saponite can also catalyse the production of organic polymers (e.g. Ferris et al. 1996; Hazen & Sverjensky 2010; Baross 2018), which are also thought to emerge from Enceladus' hydrothermal sites (Postberg et al. 2018a). An iron sulphide mineral (greigite) can reduce CO_2 to synthesize carbonyl species such as acetic acid in alkaline hydrothermal environments (Roldan et al. 2015). In experiments aimed at recreating conditions on a primordial Earth, Barge et al. (2019) hydrothermally synthesized alanine and lactate from ammonia and a low-mass carbonyl compound in the presence of iron oxyhydroxide. The experimental conditions (e.g. temperature and pH) under which these reactions occurred are again very similar to those postulated to be ongoing within Enceladus (Postberg et al. 2009a; Hsu et al. 2015; Sekine et al. 2015; Waite et al. 2017; Glein, Postberg & Vance 2018).

Based on the work of Ménez et al. (2018) and Barge et al. (2019), the presence (depending on, e.g. availability/solubility) of the low-mass aromatic, O- and/or N-bearing compounds we have identified here therefore suggests at least two reaction pathways (Fig. 7) for hydrothermal abiotic synthesis of biochemical precursors may be possible within Enceladus' ocean. The products of these reactions may then undergo polymerization (e.g. McCollom & Seewald 2007; Milesi, McCollom & Guyot 2016; Vinogradoff et al. 2018) and synthesize the macromolecular organic material identified in previous work (Postberg et al. 2018a).

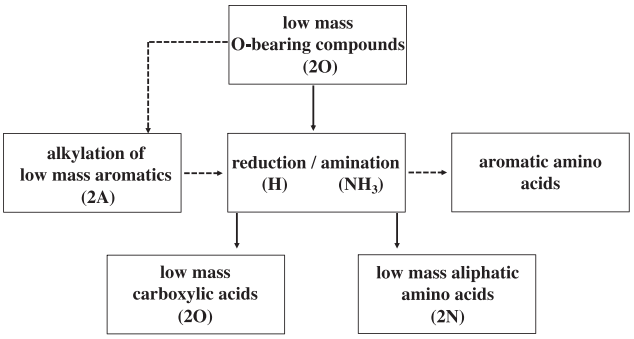

Figure 7. Different reaction pathways for the synthesis of potential biosignatures (amino acids and carboxylic acids) under Enceladean hydrothermal conditions. Here, 2O, 2A, and 2N refer to the classes of low-mass organic compounds found in Enceladus Type 2 grains. These may be precursors (low-mass carbonyls and aromatics) as well as products (low-mass carboxylic and aliphatic amino acids) of the reactions. Two main routes can involve low-mass O-bearing compounds (2O). Shown by the dashed arrows, the alkylation of available low-mass aromatics (2A) with low-mass O-bearing compounds (2O) is followed by amination. This route produces aromatic amino acids, which are intermediate-sized (described in the main text) compounds remaining dissolved in Enceladus ocean. The other route follows two pathways (in solid arrows): either reduction of precursor O-bearing compounds into low-mass carboxylic acids or reductive amination to synthesize low-mass amino acids.

The first pathway (Fig. 7) would involve Friedel–Crafts-like reactions in hydrothermal sites within Enceladus. Here, the alkylation of low-mass MAC with low-mass O-bearing (e.g. pyruvate, for which an example spectrum of Pyruvic acid is shown in the supplementary

material, Fig. SM 9) compounds, in the presence of ammonia, may produce aromatic amino acids (e.g. tryptophan). A second route (Fig. 7) requires the reductive amination of low-mass O-bearing compounds (e.g. pyruvate) to aliphatic amino acids (e.g. alanine). A further possible pathway would involve the reduction of pyruvate-like O-bearing compounds to carboxylic acids (e.g. lactic acid).

Although not a unique interpretation, many relevant precursor molecules (MACs, pyruvate-like O-bearing molecules, and small amino acids) are in agreement with the spectral features of the compositional groups (Types 2A, 2O, 2N, respectively) found in this work. This is also true for low-mass carboxylic acids (2O). NH_3 is also a major plume constituent (Waite et al. 2017) and thus probably available at Enceladean hydrothermal sites.

Our results also shed further light on the question of how organic material with differing physical properties finds its way into the plume and specifically into ice grains. Postberg et al. (2018a) postulate that the transport of Enceladus' hydrothermal material from the core is supported by both convection and bubbles from upwelling and thereby exsolving volatile gases. This collects organic material from the deep ocean and delivers it to shallower depths. The water surface to which such organics may be delivered is situated inside cracks in the less than 5 km thick south polar ice crust (Beuthe, Revoldini & Trinh 2016; Cadek et al. 2016; Le Gall et al. 2017) and from isostatic considerations (e.g. Matson et al. 2012) lies less than 1 km below Enceladus' surface (Postberg, Tobie & Dambeck 2016; Spencer et al. 2018). These reservoirs are believed to be efficiently evaporating at near triple-point conditions (Schmidt et al. 2008; Postberg et al. 2009a; Yeoh et al. 2015).

Current understanding of the formation of ice grains inside Enceladus that are then ejected into the plume invokes two simultaneous mechanisms (Fig. 8). Nearly pure water ice grains (producing Type 1 spectra) can form from condensation of supersaturated vapour inside and above the ice vents (Schmidt et al. 2008; Postberg et al. 2009a; Yeoh et al. 2015). However, salty ice grains (Type 3) are thought to be frozen ocean spray generated by turbulence within the fractures (Kite & Rubin 2016) and/or when bubbles reach the water surface located inside vertical cracks in the crustal ice, and burst (Postberg et al. 2009a; Matson et al. 2012). The bubbles are formed either from water vapour produced by boiling water close to its triple point, or upwelling volatile gases [e.g. CO_2 (Matson et al. 2012), CH_4, or H_2 (Waite et al. 2017)]. If the droplets produced in the spray are smaller than a few micrometres, thermal support against gravity in the water vapour is possible, at gas densities slightly below the triple point. The droplets are then carried through the ice vents with the vapour from the evaporating water, following the pressure gradient into space.

Grains with particularly high concentrations of poorly soluble and probably hydrophobic organic material with molecular masses above 200 u discussed in Postberg et al. (2018a) are thought to be formed from a thin layer, enriched with insoluble organic material, on the water surface. Bursting bubbles disperse the organic layer and, in a process analogous to that which forms the salty ocean spray (Lhuissier & Villermaux 2012), form an organic spray, which then acts as nucleation cores for subsequent coating by condensing water vapour when ascending though a fracture into space (Postberg et al. 2018a) (Fig. 8).

Our analysis of low-mass organic material in this work contributes new key aspects (Fig. 8). In contrast to the aforementioned high-mass organics, these polar and hydrophilic N- and O-bearing compounds are unlikely to be phase separated from water and were therefore previously dissolved in the Enceladean ocean. Another crucial difference to the macromolecular organic compounds discussed in Postberg et al. (2018a) is that at the water surface they can be efficiently volatilized in the low-pressure environment within Enceladus' crustal fractures (Fig. 8). The volatile organic compounds (VOCs) will then follow the pressure gradient towards open space, flowing upwards with the water vapour through the fractures. During the ascent in these ice vents, ambient temperatures drop from about 272 K near the water table to ∼200 K at even the hottest outlets (Goguen et al. 2013). Exposed to such temperature drops (Schmidt et al 2008; Yeoh et al. 2015), VOCs recondense on to the pre-existing (Fig. 8), but still growing, ice grains that act as efficient nucleation cores. Bouquet, Glein & Waite (2019) investigated the effect of adsorption of VOCs on to the ice vent walls and grains ejected in the Enceladus' plume. The study showed a predominance of VOCs in the ice phase if their molecular binding energies (energy of desorption) are greater or equal to 0.7 eV, indicating VOCs in the gas phase detected by INMS and those detectable by CDA in ice grains can differ in composition and concentration. Bouquet et al. also revealed that polar O-bearing VOCs, with the exception of formaldehyde, accumulate more efficiently than pure hydrocarbons on to ice grains. Number concentrations with respect to water molecules in the grains were estimated to be approximately 0.2 per cent. The grains enriched with N- and O-bearing polar VOCs ejected from Enceladus are thus detected by CDA, whereas other less polar VOCs, for which grain condensation is less energetically favourable, remain unaltered in the gas phase until emission from Enceladus, and are detected by Cassini's INMS.

Magee & Waite (2017) have identified candidate organic compounds emerging from Enceladus' ocean and detected in the gas plume with varying levels of ambiguity in the composition of these species (Postberg et al. 2018b). The compounds with a moderate level of ambiguity cover the mass range ∼24–34 u. This is approximately equivalent to CDA's mass range (∼26–31 u) in the LMOS region (Section 1), where the species are indistinguishable in Type 2 spectra (Fig. 1). In this mass range and ambiguity level, Bouquet et al. (2019) only discussed the adsorption of acetylene (C_2H_2), Ethylene (C_2H_4), and Formaldehyde (CH_2O) on to the ice grains. These compounds have much lower binding energies with ice ($E_{\rm des} \sim \leq 0.4$ eV) than the 0.5 eV lower limit discussed by Bouquet et al. (2019), and therefore cannot be adsorbed on to ice grains despite their high vapour pressures (e.g. ≥100 kPa at 273 K). However, methanol, detected with high ambiguity by Magee & Waite (2017), is also discussed by Bouquet et al. (2019), has a binding energy of $\sim 0.52 \pm 0.06$ eV, and might be adsorbed on to ice grains in trace amounts. In the laboratory, methanol produces an M+H peak at 33 u, and although it does not produce a peak in the LMOS region, it may contribute to a broadening of this feature at higher masses. However, no dominant peak at 33 u has so far been identified and therefore we suggest that most of the organic molecular compounds in the mass range ∼24–34 u as identified by Magee & Waite (2017) remain in the gas phase and hence are absent in CDA spectra. By extension, the ions contributing to the LMOS peak in CDA Type 2 spectra are thus more likely to be fragments of larger molecules.

Magee and Waite (2017) have also suggested chemical formulae for organic compounds seen in INMS spectra, albeit with high ambiguity in their identification, with molecular masses $\sim \geq 33$ u, classified into different groups: O-bearing, N-bearing, NO-bearing, halogenated organics as well as hydrocarbons. Mass lines stemming from many of these organic compounds are used to explain INMS spectral features at masses of between 36 and 46 u. From the spectra investigated in this work, in combination with Magee and Waite's

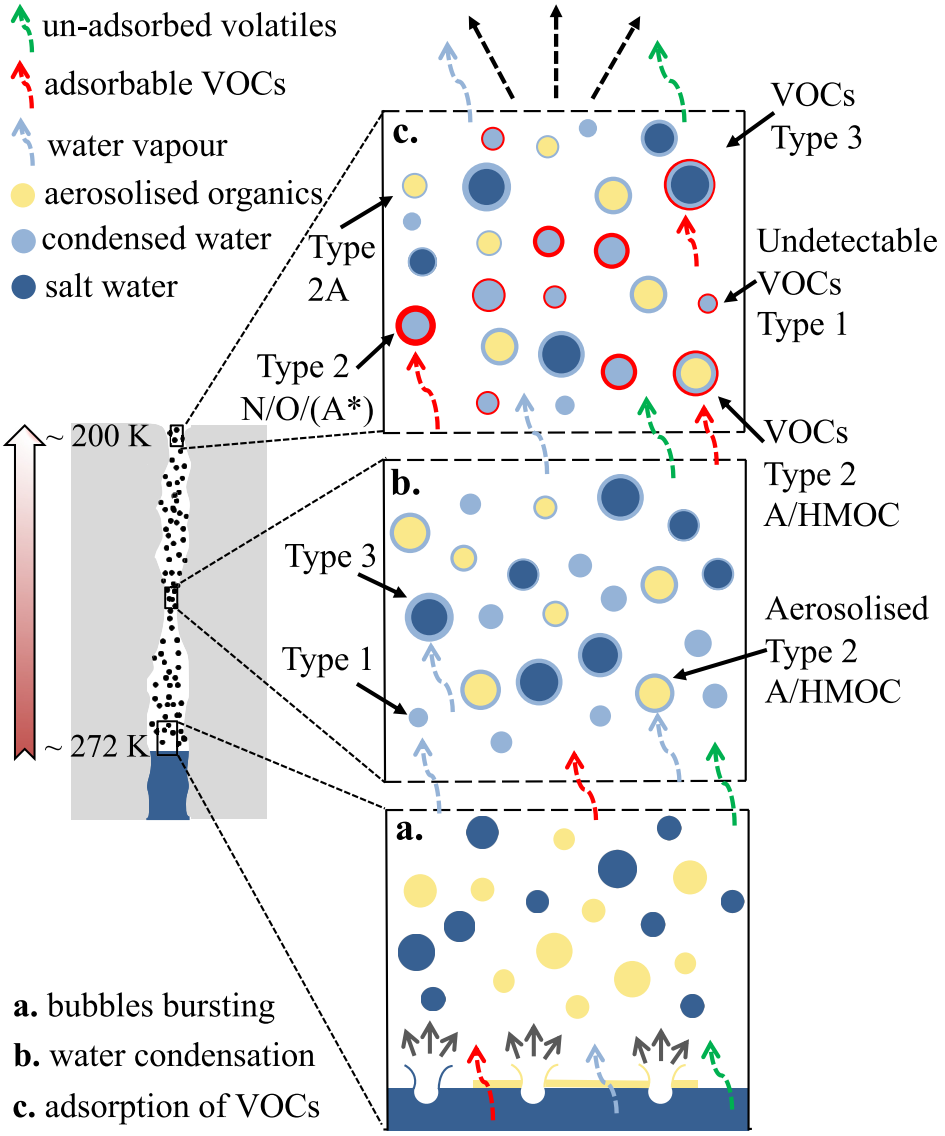

Figure 8. Overview (not to scale) of different mechanisms for the formation of ice grains inside Enceladus' south polar ice vents. The **left-hand** panel shows the upper part of an ice crack and an approximate location for the water table. The general temperature trend, cooling towards the surface, is shown by the arrow to the left. At the salt water surface, the temperature is about 272 K, gradually decreasing to approximately 200 K just before the ice grains enter space. In the **right-hand** three panels, grain formation and evolutionary processes, occurring at different regions in the vents, are shown. With the exception of the bubble bursting process (a), grain formation and evolution may occur at various depths within the fractures but here are shown in discrete locations (b, c) for clarity. The coloured dashed arrows represent different volatile species (water vapour, unadsorbent, and adsorbent VOCs shown by blue, green, and red, respectively). Different processes of grain formation and growth are shown: (i) bursting of upwelling gas bubbles at the water surface, aerosolizing salty water and an insoluble organic layer, (ii) condensation of salt-poor water ice from vapour, and (iii) adsorption of volatile organic species on to ice grains. Grains and surface layers are not shown to scale. **(a) Bubble bursting:** Water vapour and gas bubbles exsolve or upwell, and burst at the water surface. This creates a spray of not only salt-water aerosols (Postberg et al. 2009a) from the ocean (both dark blue) but also loft droplets of organic material (yellow) present as a layer at the water surface, including low-mass insoluble Type 2A compounds if present and/or Type 2 HMOC compounds (Postberg et al. 2018a). The dashed arrows represent volatile species that form the gaseous component of Enceladus' plume. **(b) Water condensation:** Here water vapour becomes supersaturated at a narrow neck of the ice vent (Schmidt et al. 2008). Water vapour (light blue dashed arrow) condenses to form almost pure water ice grains (light blue, **Type 1**) and also condenses on to salt-water aerosols (dark blue) and aerosolized organic droplets (yellow), both of which act as nucleation cores, forming **Type 2 A/HMOC** ice grains and salt-rich **Type 3** grains. We considered here the insoluble case of aromatic subtype 2A. Minor quantities of volatile organic species (in red) may also adsorb here but are not shown at this stage for clarity. These VOCs are more efficiently adsorbed at lower temperatures and are thus shown in panel (c). **(c) Adsorption of volatile organics:** Volatile organic species (N- and O-bearing) with high binding energies (Bouquet et al. 2019) and/or condensation temperatures below 200 K can adsorb on to all pre-existing ice grains (Type 1, Type 2A, Type 2 HMOC, and Type 3) in the vent. Type 1 grains may therefore convert to **Type 2 N/O** grains if a detectable amount of volatile organics is adsorbed (bold/wide circles in red) or with only undetectable amounts of volatiles (thin red circles) remain as Type 1. Low-mass insoluble aromatic grain (yellow with thin light blue circle) without any VOCs is marked as Type 2A. Low-polarity volatile gases with low binding energy and high condensation temperature (green dashed arrows) are not adsorbed on to ice grains and remain unaltered in the gas phase leaving the vents together with uncondensed water vapour (blue dashed arrows). Despite the INMS non-detection of aromatic compounds, we cannot completely rule out the creation of Type 2A via adsorption from the vapour phase, here indicated by A*.

Table 2. O- and N-bearing organic compounds selected (full list SM Table 6) from Magee & Waite (2017) that might condense on to ice grains sorted by different levels of grain vapour deposition likelihood, based on the criteria given in the main text. ∗The binding energies for amorphous ice are applied for these species. ∗∗We estimate that these NO-bearing species are more likely to produce O-bearing fragments.

Level of certainty	O-bearing	N-bearing
Level 1 (a,b,e)	acetic acid: $C_2H_4O_2$	–
Level 2 (a,c,e)	∗acetaldehyde: C_2H_4O	methylamine: CH_5N
Level 3 (a,d,e)	vinyl acetate: $C_4H_6O_2$	
	ethylene oxide: C_2H_4O	ethylamine/dimethylamine: C_2H_7N
	propanal/propylene oxide: C_3H_6O	
	ethyl methyl ether: C_3H_8O	
	2-butanol/isopropyl methyl ether: $C_4H_{10}O$	
	2,3-butanedione: $C_4H_6O_2$	
	∗∗ethyl nitrite: $C_2H_5NO_2$	
	∗∗isopropyl nitrite: $C_3H_7NO_2$	

tentative identifications, and the binding energies presented by Bouquet et al. (2019) as well as inferred from Wakelam et al. (2017) and Szentermai et al. (2016), we can estimate the likelihood that the species identified in the gas phase are responsible for producing the Type 2O, 2N, and 2A spectra after adsorption on to ice grains in the vents. Species can therefore be discounted (Table SM 6) due to one or more of the following:

1. If they produce spectral features not in agreement with Type 2O, 2N, or 2A – e.g. aliphatic hydrocarbons and O- and N-bearing species with C > 4.
2. If they have a binding energy with crystalline water ice known to be less than 0.5 eV or with amorphous water ice <0.42 eV.
3. If they have an unsuitable vapour pressure at ∼273 K.

However, binding energies are not well constrained for most of the species given in Magee and Waite (2017), and the exact vapour pressure threshold for entry into the plume is also poorly known. We therefore classify the ability of the compounds to enter grains from the vapour phase into three levels of likelihood (Table 2), based on combinations of the following criteria:

(a) Spectral appearance: Characteristic cations are observed in their spectra, or if spectra are not available, the structure of the compound is expected to produce suitable characteristic cations following molecular cleavage.
(b) Binding energies: ≥0.7 eV.
(c) Binding energies: between 0.5–0.7 eV for crystalline ice and 0.42–0.7 eV for amorphous ice (see SM section D).
(d) Binding energies: unavailable.
(e) Vapour pressure: ≥0.31 kPa (half of the water vapour pressure) at 273 K.

We suggest suitable candidates for the Type 2N and 2O species (Table 2). Acetic acid is the *only* candidate that definitely meets the criteria for O-bearing VOCs entering the particles via the gas phase. Aldehydes are also good candidates for this mechanism. Other possible species for which we could not find binding energies include ketones, ethers, and nitrites**.** Interestingly, for the Type 2N grains, we find that amines are the only possible compounds that could enter grains this way whilst agreeing with the combined observations of INMS and CDA.

Depositing from the vapour/gas phase, the O- and N-bearing species would also be expected to be present in all ice grains, including those particles which give rise to pure water Type 1 spectra and which do not show organic signatures (Postberg et al. 2009a, 2011). Indeed, the transition between Type 1 and Type 2 spectra of ice grains is continuous. For example, many Type 1 spectra show indications of an LMOS feature with a signal-to-noise ratio below the 2.5σ level, disqualifying these spectra from inclusion in the Type 2 data set. The fraction of Type 2 detections generally significantly increases in proportion to the overall strength of the spectral signal (i.e. the total ion yield) with the best signal-to-noise ratio, whereas the fraction of Type 1 detections decreases (Postberg et al. 2008, 2011, 2018b). This may indicate that most, if not all, ice grains emitted by Enceladus contain organic condensates at varying concentrations, the detection of which, above the noise level, is only possible for CDA when a particular organic cation signal is strong enough. Thus, the detection, and with it the classification into Types 1 and 2, depends on the absolute number of organic ions contributing to a signal at a given molecular mass. This quantity is more related to the absolute abundance of an organic species in an ice grain than to its concentration.

The vapour condensation process is also expected to occur on to the surfaces of salty ice grains (Type 3), previously formed from oceanic aerosols, as they are entrained in the outgassing vapour. Although there are indications in the CDA data for such grains, our focus in this work, on spectra with simple, diagnostic features, means organic signatures from salt-rich grains are beyond our scope. The biochemical precursors produced by the processes described earlier, and summarized in Fig. 7, although polar and soluble, would be more massive than the VOCs identified in this work, and intermediate in mass between the VOCs and the HMOC compounds. They are therefore not expected to be detected in Type 2 grains, as their solubility and low vapour pressures mean they will remain dissolved within the ocean, but are instead likely to be found in the Type 3 grains. We note, however, that alkali metal salts are known to modify and/or suppress organic signatures and instigate strong matrix effects (Piwowar et al. 2009; Klenner et al. 2018), complicating the (ongoing) identification of these intermediate-mass organics.

The single-ringed aromatic compounds that do not result in an HMOC pattern in spectra and are identified in this work as Type 2A may, in principle, form via a similar mechanism to the other Type 2 grains, by incorporation of organics into the ice grains by evaporation and recondensation. Volatilization of the observed aromatic compounds may occur directly from the ocean surface if the compounds are at least sparingly soluble or if they evaporate from an insoluble layer on the water surface that is thought to be rich in more complex aromatic constituents (Postberg et al. 2018a).

For example, benzene (vapour pressure at 0°C ∼ 3500 Pa) can efficiently be volatilized at the triple point of water occurring at 612 Pa, a pressure thought to be representative of the region directly next to Enceladus' water surface (Schmidt et al. 2008). However, to date, INMS has not detected benzene in the plume gases (e.g. Magee & Waite 2017; Postberg et al. 2018b). This non-detection may be due to instrument sensitivity, with INMS 'averaging' out the composition of the Enceladean plume, or because of a real lack of benzene at the time of measurement – whether permanent or arising from temporary changes in plume composition. Other more soluble candidates, such as phenol, which is more polar than benzene and likely to have a higher binding energy with water ice, may have vapour pressures (e.g. ∼3 Pa for phenol) too low for entry into the plume in appreciable quantities, and thus also be undetectable by INMS. Alternatively, low-vapour pressure compounds, whether poorly soluble or insoluble, could also form Type 2A grains via the same heterogeneous nucleation process as HMOC-type grains, in which bursting bubbles loft organic compounds as droplets, which then act as efficient condensation cores. Although the absence of identified molecular peaks argues against this scenario, the infrequent presence of a low-resolution feature in the extended mass region (above 200 u) of the CDA spectra, may support the occasional occurrence.

In hydrothermal reactions (e.g. Friedel–Crafts reactions) polar, low-mass and initially dissolved aromatic compounds may change their polarity and become less soluble and reactive. These low-mass aromatics could then be transported from the depths of Enceladus ocean towards the surface and then incorporated into Type 2A grains via aerosolization. In this way, the aromatic organics could also be mixed with the more volatile organics (e.g. O- and N-bearing) and result in grains that give rise to the mixed-type spectra (Table 1). Mixing of HMOC material with O- and N-bearing volatile compounds could occur in a similar way.

Organic-enriched ice grains show strong grain-to-grain variation in their compositions and the apparent abundance of organics within the grains. These differences may be indicative of variations in the environmental conditions within the south polar fractures on Enceladus. Emission of icy dust, gas, and vapour from the south polar is a dynamic process, with both temporal and spatial variation in grain production and size distribution. Enceladus' plume activity is linked to tidal flexure of the fractures (e.g. Hedman et al. 2013; Kite & Rubin 2016; Ingersoll & Ewald 2017), and possibly subsurface water motion and fracture tortuosity (Teolis et al. 2017). The infrared spectra of emitted ice grains are also known to vary between different 'Tiger Stripe' fractures (Dhingra et al. 2017), perhaps due to variations in formation environments and fracture geometries. We consider it therefore probable that the variations observed in the composition and abundance of organic-enriched ice grains at least partially arise from similar processes.

7 CONCLUSIONS

In this study, we have characterized CDA spectra of organic-bearing ice grains (Type 2) and inferred structural information concerning low-mass organic species. We used a subset of spectra with particularly pronounced organic signatures to identify three specific spectral subtypes attributable to the presence of different organic cations. To identify these signatures and the parent molecules that give rise to them, we have investigated mass spectra from suitable analogue materials in a water matrix in the laboratory. There the impact ionization process of ice grains is simulated by a pulsed IR laser firing on an ultrathin water beam (Postberg et al. 2009a, Klenner et al. 2019).

Four key diagnostic cations – NH_4^+ (ammonium), $C_2H_{3,5}O^+$ (acylium and/or ethoxy), and $C_6H_5^+$ (phenyl) – were used to classify N-bearing and O-bearing aliphatic, as well as single-ringed aromatic, compounds in the ice grains, all with molecular masses below 100 u. Based on the laboratory experiments, the N-bearing signatures in Type 2N stem from amines, nitriles, and/or amides whereas the O-bearing signatures in Type 2O can be reconciled with aldehydes, ketones, carboxylic acids, alcohols, or ethers. Finally, we find phenyl- and benzoyl-like compounds to be the most suitable candidates for the low-mass aromatic signatures in subtype 2A.

Our data suggest that aliphatic N-bearing and O-bearing compounds in the grains originate from low-mass hydrophilic VOCs that probably were previously dissolved in the ocean. We suggest that most of these compounds efficiently evaporate from Enceladus' oceanic water and subsequently recondense and adsorb (Postberg et al. 2018b; Bouquet et al. 2019) on to water ice nucleation cores upon cooling during ascent through the icy crustal cracks. This is not necessarily the case for the aromatic subtype, where the candidate compounds are undetected in the vapour phase. Thus, we propose that they form by bubble bursting, potentially originating from an organic layer on top of the water surface as proposed by Postberg et al. (2018a).

Types 2N and 2O are formed by vapour condensation in Enceladus ice vents and so further constraints can be placed on the exact identities of compounds by comparing CDA spectra with the candidate organic molecules identified in the plume gas (Magee & Waite 2017, Postberg et al. 2018b). Thus, by considering the physical and chemical environments within the Enceladean vents as well as suitable binding energies (Bouquet et al. 2019) and vapour pressures, only a few species remain that could plausibly condense into Type 2O and 2N grains. Of these, acetic acid and acetaldehyde are excellent candidates for the production of Type 2O and amines are left as the only plausible candidates for the production of 2N grains.

The non-detection of aromatics in the gas phase by INMS implies that any progenitor species for Type 2A grains has a very low vapour pressure. Of the species so far considered, phenol, aniline, benzoic acid, and styrene-like compounds are therefore considered more likely than benzene and, if poorly soluble, or insoluble, could be present as a separate phase and are likely to enter grains via bubble bursting. In comparison to Types 2O and 2N, the exact identification of such species, and therefore the precise formation mechanism of Type 2A grains, is highly ambiguous, not least as no obvious molecular peak candidates have so far been found. We also cannot completely rule out the – undetected by INMS, and perhaps temporally or spatially variable – presence of benzene in the gas phase, with VOC-like adsorption pathways into E ring ice grains then possible.

The organic concentrations within the selection of ice grain spectra discussed in this work are estimated to be at least at the mmol level, in broad agreement with the value (0.2 per cent by number with respect to water) calculated by Bouquet et al. (2019). However, we used CDA spectra exhibiting only the most clearly and unambiguously identifiable signatures as archetypes. The identified compounds probably reside in many more, if not most, of the ice grains, although in highly variable and often much lower concentrations. Owing to the limitations of the CDA spectral quality and possible isobaric interferences with other particle constituents, especially water clusters, the presence of further, so far unidentified, organic species is highly probable.

Furthermore, we reinvestigated the CDA data set of Postberg et al. (2018a) exhibiting features generated by high-mass complex organics. Through the attribution of additional spectral characteristics, we confirm the tentative identification of N-bearing species in HMOC spectra (Fig. SM 7) and further affirm their finding that O-bearing species are present (Fig. SM 8). In these cases (Table SM 5), it is possible that O- and N-bearing functional groups originate directly from the HMOC parent molecules.

The observed variations in the concentration and composition of organic compounds in particles may be the result of variations in subsurface oceanic as well as fracture conditions, leading to differing formation and evolutionary conditions as grains are generated and grow. The condensation of pure water grains is difficult to reconcile with an organic-rich plume, unless there is significant fracture to fracture variation in the composition of the plume gas, with some fractures entirely free of adsorbable organic vapour/gas.

It is therefore possible, perhaps even very likely, that the vast majority of grains emitted from Enceladus contain VOCs, with the distinction between Type 1 and Type 2 purely the result of VOC abundance, instrument effects (e.g. noise limitations, increased sensitivity to minor compounds at higher impact velocities), and the selection effect introduced by signal-to-noise requirements for LMOS peak identification. The LMOS peak is the sole distinguishing criterion between the otherwise very similar Type 1 and Type 2 spectra. Larger grains naturally will carry a higher organic volatile content (not necessarily concentration), which will then be more likely to overcome the detection and classification threshold in CDA mass spectra. Therefore, Type 1 and those Type 2 grains forming from volatile condensation might just be the small and large populations, respectively, of nearly identically composed grains. Hints of just such a size distribution difference between Type 1 and Type 2 grains have indeed been found (Hillier et al. 2007; Postberg et al. 2008, 2009a).

We have demonstrated that one can probe the organic inventory of Enceladus' – probably hydrothermal – core by *in situ* analysis of material ejected into the plume or the E ring. The abiotic synthesis of N-containing aliphatic (Barge et al. 2019) and aromatic (Ménez et al. 2018) amino acids, as found in the Lost City hydrothermal site (Ménez et al. 2018), may be relevant to the geo-chemical and physical environment of Enceladus. We propose that the reactive low-mass organic material identified in this work can take part in similar synthesis pathways, generating such biologically relevant organic compounds with intermediate masses between those of the VOCs and the HMOC material. Indeed, retrosynthesis of glycine and alanine has revealed that the low-mass N-bearing species (methylamine and ethylamine) we identify as the most suitable candidates for the Type 2N compound(s) are potential precursors of these proteinogenic amino acids (Vallentyne 1964; Förstel et al. 2017). Further processing, including polymerization reactions, may then result in the production of, or contribution to, the detected HMOC complex macromolecular organic compounds.

It is highly likely that there are many more dissolved organic compounds in the Enceladean ocean than reported here (Kahana, Schmitt-Kopplin & Lancet 2019). In this investigation of Type 2 grains, the initial constraints, in particular the choice of salt-poor spectra, favoured the identification of compounds with high vapour pressures. Despite the expected solubility of potential synthesized intermediate- or high-mass compounds, their low vapour pressures mean that they will not efficiently evaporate at the water surface and thus remain undetectable not only in the vapour, but also those Type 2 grains forming from it. Potential soluble biosignatures with higher masses might therefore be found in spectra from Type 3 grains, which are thought to form from oceanic spray (Postberg et al. 2009a, 2011). Finding and identifying such biosignatures will be the main goal of future work. The putative low vapour pressure, higher mass, dissolved organics might also be enriched in the organic near-surface layer postulated by Postberg et al. (2018a) and thus might also enter HMOC-type ice grains.

Similarities between the hydrothermal environments in Enceladus and on the Earth, where life might have developed without sunlight, reinforce the importance of further exploring Enceladus' habitability. Cassini's CDA, despite its substantial achievements, was not designed for this task. A future space mission with a dedicated payload of modern, high-resolution mass spectrometers (Lunine 2016; Reh et al. 2016; Mitri et al. 2017) would be able to deliver a dramatic improvement in the characterization of Enceladus' rich organic chemistry and, with that, our understanding of the habitability of Enceladus' subsurface ocean.

ACKNOWLEDGEMENTS

The work was supported by the German Research Foundation (DFG) under projects PO 1015/2-1, /3-1, /4-1, an European Research Council (ERC) Consolidator Grant 724908-Habitat OASIS, and the German Space Agency under DLR grant 50OH1501.

REFERENCES

Alexander C.O'.D., Cody G. D., De Gregorio B. T., Nittler L. R., Stroud R. M., 2017, Geochemistry, 77, 227
Barge L. M., Flores E., Baum M. M., VanderVelde D. G., Russel M. J., 2019, Proc. Natl. Acad. Sci., 116, 4828
Baross J. A., 2018, Nature, 564, 42
Beuthe M., Rivoldini A., Trinh A., 2016, Geophys. Res. Lett., 43, 10088
Bouquet A., Glein C. R., Waite J. H., 2019, ApJ, 873, 13
BurattiB. J. et al., 2019, Science, 364, 1126
Čadek O. et al., 2016, Geophys. Res. Lett., 43, 5653
Choblet G., Tobie G., Sotin C., Behounkova´ M., Cadek O., Postberg F., Soucek O., 2017, Nat. Astron., 1, 841
Dhingra D., Hedman M. M., Clark R. N., Nicholson P. D., 2017, Icarus, 292, 1
Donsig H. A., Vickerman J. C., 1997, Chem. Soc. Faraday Trans., 93, 2755
Dougherty M. K., Khurana K. K., Neubauer F. M., Russell C. T., Saur J., Leisner J. S., Burton M. E., 2006, Science, 311, 1406
Ferris J. P., Hill A. R., Jr Liu R., Orgel L. E., 1996, Nature, 381, 59
Förstel M., Bergantini A., Maksyutenko P., Gobi S., Kaiser R. I., 2017, ApJ, 845, 83
Glein C. R., Postberg F., Vance S. D., 2018, in Schenk P. M., Clark R. N., Howett C. J. A., Verbiscer A. J., Waite J. H., eds, Enceladus and the Icy Moons of Saturn. Univ. Arizona, Tucson, USA, p. 39
Goguen J. D. et al., 2013, Icarus, 226, 1128
Hansen C. J., Esposito L., Stewart A. I. F., Colwell J., Hendrix A. R., Pryor W. R., Shemansky D., West R., 2006, Science, 311, 1422
Hansen C. J. et al., 2011, Geophys. Res. Lett., 38, 1
Hazen R. M., Sverjensky D. A., 2010, Cold Spring Harb. Perspect. Biol. 2, a002162
He J., Acharyya K., Vidali G., 2016, ApJ, 825, 89
Hedman M. M. et al., 2013, Nature, 500, 182
Henderson B. L., Gudipati M. S., 2015, ApJ, 800, 66
Hillier J. K. et al., 2007, MNRAS, 377, 1588
Hsu H. W. et al., 2015, Nature, 519, 207
Ingersoll A. P., Ewald S. P., 2017, Icarus, 282, 260
Kahana A., Schmitt-Kopplin P., Lancet D., 2019, Astrobiology, 19, 1
Kempf S., Beckmann U., Schmidt J., 2010, Icarus, 206, 446
Kempf S., Horányi M., Hsu H.-W., Hill T. W., Juhász A., Smith H. T., 2018, in Schenk P. M., Clark R. N., Howett C. J. A., Verbiscer A. J., Waite J.

H., eds, Enceladus and the Icy Moons of Saturn. Univ. Arizona, Tucson, USA, p. 195
Kite E. S., Rubin A. M., 2016, Proc. Natl. Acad. Sci., 113, 3972
Klenner F., Postberg F., Stolz F., Khawaja N., Reviol R., 2018, EPSC, 12, 1262
Klenner F. et al., 2019, Rapid Commun. Mass Spectrom.
Knochenmuss R., Dubois F., Dale M. J., Zenobi R., 1996, Rapid Commun. Mass Spectrom., 10, 871
Lee T. A., 1998, A Beginner's Guide to Mass Spectral Interpretation (Vol. 01). John Wiley & Sons Ltd., West Sussex, England
Le Gall A. et al., 2017, Nat. Astron., 1, 0063
Lhuissier H., Villermaux E., 2012, J. Fluid Mech., 696, 5
Lunine J. I., 2016, Acta Astronaut., 131, 123
Magee B. A., Waite J. H., 2017, LPSC, XLVIII (2974)
Matson D. L., Castillo-Rogez J. C., Davies A. G., Johnson T. V., 2012, Icarus, 221, 53
McCollom T. M., Seewald J. S., 2007, Chem. Rev., 107, 382
McLafferty F. W., Turecek F., 1993, Interpretation of Mass Spectra (Vol.04). Univ. Sci. Books, California, USA
Ménez B. et al., 2018, Nature, 564, 59
Milesi V., McCollom T. M., Guyot F., 2016, Geochim. Cosmochim. Acta 189, 391
Mitri G. et al., 2017, Planet. Space Sci., 155, 73
Piwowar A. M., Lockyer N. P., Vickerman J. C., 2009, Anal. Chem., 81, 1040
Porco C. C. et al., 2006, Science, 311, 1393
Postberg F., Kempf S., Hillier J. K., Srama R., Green S. F., McBride N., Grün E., 2008, Icarus, 193, 438
Postberg F., Kempf S., Schmidt J., Brilliantov N., Beinsen A., Abel B., Buck U., Srama R., 2009a, Nature, 459, 1098
Postberg F., Kempf S., Rost D., Stephan T., Srama R., Trieloff M., Mocker A., Goerlich M., 2009b, Planet. Space Sci. 57, 1359
Postberg F., Schmidt J., Hillier J., Kempf S., Srama R., 2011, Nature, 474, 620
Postberg F., Tobie G., Dambeck T., 2016, Sci. Am., 315, 38
Postberg F. et al., 2018a, Nature, 558, 564
Postberg F., Clark R. N., Hansen C. J., Coates A. J., Dalle Ore C. M., Scipioni F., Hedman M. M., Waite J. H., 2018b, in Schenk P. M., Clark R. N., Howett C. J. A., Verbiscer A. J., Waite J. H., eds, Enceladus and the Icy Moons of Saturn. Univ. Arizona, Tucson, USA, p. 129
Reh K., Spilker L., Lunine J. I., Waite J. H., Cable M. L., Postberg F., Clark K., 2016, Aerospace Conference, p. 1
Roldan A. et al., 2015, Chem. Commun., 51, 7501
Schmidt J., Brilliantov N., Spahn F., Kempf S., 2008, Nature, 451, 685
Sekine Y., Shibuya T., Postberg F., Hsu H.-W., Suzuki K., Masaki Y., 2015, Nat. Commun., 6, 8604
Southworth B. S., Kempf S., Spitale J., 2019, Icarus, 319, 33
Spahn F. et al., 2006a, Science, 311, 1416
Spahn F. et al., 2006b, Planet. Space Sci., 54, 1024
Spencer J. R. et al., 2006, Science, 311, 1401
Spencer J. R. Nimmo F., Ingersoll A. P., Hurford T. A., Kite E. S., Rhoden A. R., Schmidt J., Howett C. J. A., 2018, in Scheck P. M., Clark R. N., Howett C. J. A., Verbiscer A. J., Waite J. H., eds, Enceladus and the Icy Moons of Saturn. Univ. Arizona, Tucson, USA, p. 163
Srama F. et al., 2004, Space Sci. Rev., 114, 465
Szentermai V., Szori M., Picaud S., Jedlovszky P., 2016, JPCC, 120, 23480
Teolis B. D., Perry M. E., Hansen C. J., Waite J. H., Porco C. C., Spencer J. R., Howett C. J. A., 2017, Astrobiology, 17, 926
Thomas P. C., Tajeddine R., Tiscareno M. S., Burns J. A., Joseph J., Loredo T. J., Helfenstein P., Porco C., 2016, Icarus, 264, 37
Tobie G., 2015, Nature, 519, 162
Vallentyne J. R., 1964, Geochim. Cosmochim. Acta, 28, 157
Vinogradoff V., Bernard S., Le Guillou C., Remusat L., 2018, Icarus, 305, 358
Waite J. H. et al., 2006, Science, 311, 1419
Waite J. H. et al., 2009, Nature, 460, 1164
Waite J. H. et al., 2017, Science, 356, 155
Wakelam V., Loison J.-C., Mereau R., Ruaud M. 2017, Mol. Astrophys., 6, 22
Yeoh S. K., Chapman T. A., Goldstein D. B., Varghese P., Trafton L. M., 2015, Icarus, 253, 205

SUPPORTING INFORMATION

Supplementary data are available at *MNRAS* online.

Supplementary material9.pdf

Please note: Oxford University Press is not responsible for the content or functionality of any supporting materials supplied by the authors. Any queries (other than missing material) should be directed to the corresponding author for the article.

This paper has been typeset from a TEX/LATEX file prepared by the author.